AFRL-OSR-VA-TR-2015-0100

Comprehensive Space-Object Characterization

Sudhakar Prasad
UNIVERSITY OF NEW MEXICO

04/17/2015
Final Report

Air Force Research Laboratory
AF Office Of Scientific Research (AFOSR)/ RTB
Arlington, Virginia 22203
Air Force Materiel Command

REPORT DOCUMENTATION PAGE

Form Approved
OMB No. 0704-0188

PLEASE DO NOT RETURN YOUR FORM TO THE ABOVE ORGANIZATION.

1. REPORT DATE *(DD-MM-YYYY)*	2. REPORT TYPE	3. DATES COVERED *(From - To)*
04-10-2015	Final	07/15/2011 - 01/14/2015

4. TITLE AND SUBTITLE
Comprehensive Space Object Characterization using Spectrally Compressive Polarimetric Sensing

5a. CONTRACT NUMBER

5b. GRANT NUMBER
FA9550-11-1-0194

5c. PROGRAM ELEMENT NUMBER

6. AUTHOR(S)
Profs. Sudhakar Prasad, Robert Plemmons, and David Brady

5d. PROJECT NUMBER

5e. TASK NUMBER

5f. WORK UNIT NUMBER

7. PERFORMING ORGANIZATION NAME(S) AND ADDRESS(ES)
Contracts and Grants Accounting, Main
1 University of New Mexico, MSC01 1245
Albuquerque, NM 87131

8. PERFORMING ORGANIZATION REPORT NUMBER

9. SPONSORING/MONITORING AGENCY NAME(S) AND ADDRESS(ES)
Air Force Office of Scientific Research
875 N. Randolph St., Rm 3112
Arlington, VA 22203

10. SPONSOR/MONITOR'S ACRONYM(S)
AFOSR/RSE

11. SPONSOR/MONITOR'S REPORT NUMBER(S)

12. DISTRIBUTION/AVAILABILITY STATEMENT
DISTRIBUTION A

13. SUPPLEMENTARY NOTES

14. ABSTRACT
Among the most important accomplishments of the project are
1. Development of physical models that predict how surface roughness, texture, and shape alter the state of polarization of solar illumination scattered/reflected by a space object and their use to determine surface shape, material composition, and texture;
2. Derivation and application of a number of approximate, task-based theoretical performance-assessement tools based on statistical information and Bayesian error analysis that are numerically efficient and generally applicable to image analysis, recovery, and reconstruction tasks;
3. Design, fabrication, and testing of two polarimetrically enhanced versions of the CASSI instrument using polarization sensitive elements;
4. Development and benchmarking of new algorithms for highly resolved spatial segmentation, material identification, shape determination, surface characterization, and extraction of rigid-body kinematics from polarimetric CASSI data; and
5. Recovery of 3D shape, rigid-body kinematics, and surface characterization from a time series of 2D compressive spectral-polarimetric images.

15. SUBJECT TERMS
Compressed spectral-polarimetric sensing, shape parameterization and reconstruction, Bayesian image analysis, statistical information, computational imaging, fundamental error and performance bounds, regularized image reconstruction algorithms

16. SECURITY CLASSIFICATION OF:			17. LIMITATION OF ABSTRACT	18. NUMBER OF PAGES	19a. NAME OF RESPONSIBLE PERSON
a. REPORT	b. ABSTRACT	c. THIS PAGE			Prof. S. Prasad
U	U	U	UU	25	19b. TELEPHONE NUMBER *(Include area code)* 505-277-5876

Reset

INSTRUCTIONS FOR COMPLETING SF 298

1. REPORT DATE. Full publication date, including day, month, if available. Must cite at least the year and be Year 2000 compliant, e.g. 30-06-1998; xx-06-1998; xx-xx-1998.

2. REPORT TYPE. State the type of report, such as final, technical, interim, memorandum, master's thesis, progress, quarterly, research, special, group study, etc.

3. DATES COVERED. Indicate the time during which the work was performed and the report was written, e.g., Jun 1997 - Jun 1998; 1-10 Jun 1996; May - Nov 1998; Nov 1998.

4. TITLE. Enter title and subtitle with volume number and part number, if applicable. On classified documents, enter the title classification in parentheses.

5a. CONTRACT NUMBER. Enter all contract numbers as they appear in the report, e.g. F33615-86-C-5169.

5b. GRANT NUMBER. Enter all grant numbers as they appear in the report, e.g. AFOSR-82-1234.

5c. PROGRAM ELEMENT NUMBER. Enter all program element numbers as they appear in the report, e.g. 61101A.

5d. PROJECT NUMBER. Enter all project numbers as they appear in the report, e.g. 1F665702D1257; ILIR.

5e. TASK NUMBER. Enter all task numbers as they appear in the report, e.g. 05; RF0330201; T4112.

5f. WORK UNIT NUMBER. Enter all work unit numbers as they appear in the report, e.g. 001; AFAPL30480105.

6. AUTHOR(S). Enter name(s) of person(s) responsible for writing the report, performing the research, or credited with the content of the report. The form of entry is the last name, first name, middle initial, and additional qualifiers separated by commas, e.g. Smith, Richard, J, Jr.

7. PERFORMING ORGANIZATION NAME(S) AND ADDRESS(ES). Self-explanatory.

8. PERFORMING ORGANIZATION REPORT NUMBER. Enter all unique alphanumeric report numbers assigned by the performing organization, e.g. BRL-1234; AFWL-TR-85-4017-Vol-21-PT-2.

9. SPONSORING/MONITORING AGENCY NAME(S) AND ADDRESS(ES). Enter the name and address of the organization(s) financially responsible for and monitoring the work.

10. SPONSOR/MONITOR'S ACRONYM(S). Enter, if available, e.g. BRL, ARDEC, NADC.

11. SPONSOR/MONITOR'S REPORT NUMBER(S). Enter report number as assigned by the sponsoring/ monitoring agency, if available, e.g. BRL-TR-829; -215.

12. DISTRIBUTION/AVAILABILITY STATEMENT. Use agency-mandated availability statements to indicate the public availability or distribution limitations of the report. If additional limitations/ restrictions or special markings are indicated, follow agency authorization procedures, e.g. RD/FRD, PROPIN, ITAR, etc. Include copyright information.

13. SUPPLEMENTARY NOTES. Enter information not included elsewhere such as: prepared in cooperation with; translation of; report supersedes; old edition number, etc.

14. ABSTRACT. A brief (approximately 200 words) factual summary of the most significant information.

15. SUBJECT TERMS. Key words or phrases identifying major concepts in the report.

16. SECURITY CLASSIFICATION. Enter security classification in accordance with security classification regulations, e.g. U, C, S, etc. If this form contains classified information, stamp classification level on the top and bottom of this page.

17. LIMITATION OF ABSTRACT. This block must be completed to assign a distribution limitation to the abstract. Enter UU (Unclassified Unlimited) or SAR (Same as Report). An entry in this block is necessary if the abstract is to be limited.

Final Report

Comprehensive Space Object Characterization using Spectrally Compressive Polarimetric Sensing

Prof. S. Prasad, U. New Mexico, PI
with contributions from the co-PIs,
Prof. R. Plemmons, Wake Forest U., and Prof. D. Brady, Duke U.

April 8, 2015

Period of Performance: July 14, 2011 - January 14, 2015

Grant No. FA9550-11-1-0194

Abstract

This document represents the final report on the various scientific activities and accomplishments relating to Grant No. FA9550-11-1-0194 over its period of performance, July 14, 2011 - January 14, 2015. The project had the following five overarching technical objectives, which have been re-organized under three broader categories, namely theoretical, experimental, and computational objectives and accomplishments therein:

1. To develop physical models that predict how surface roughness, texture, and shape alter the state of polarization of solar illumination scattered/reflected by a space object;
2. To develop enhanced but approximate, task-based theoretical performance-assessement tools based on statistical information and Bayesian error analysis that are numerically efficient, polynomially scalable, and generally applicable to image analysis, recovery, and reconstruction tasks; and to compare the actual performance of algorithms with theoretical bounds predicted by the above tools and to explore ways of improving performance by identifying information bottlenecks and weak links.

3. To design, fabricate, and test a polarimetrically enhanced version of the existing SD-CASSI instrument with simple polarization sensitive elements added to the beam train to generate spectrally compressive polarimetric data;
4. To develop and benchmark new algorithms for highly resolved spatial segmentation, material identification, shape determination, surface characterization, and extraction of rigid-body kinematics from polarimetric data acquired with a compressive spectral imaging system like CASSI;
5. To perform an exhaustive analysis of a newly proposed technique for the recovery of 3D shape, rigid-body kinematics, and surface characterization from a time series of 2D spectrally compressive polarimetric images;

Over its forty-two-month performance period, the research grant has supported, in part, the production of 25 publications (15 refereed and 10 conference), 2 completed PhD dissertations at UNM (Srikanth Narravula - defended in May 2014; Rakesh Kumar - defended on April 2, 2015), 1 partially completed PhD dissertation at Duke (Tsung-Han Tsai - supervised by Prof. D. Brady), 15 professional presentations (10 invited, 5 contributed), and 1 US patent application. Based on research partially supported by the grant, 2 additional manuscripts are currently in preparation for submission to peer-reviewed journals.

1 Summary of Overall Project Accomplishments

The following is a list of the most important technical accomplishments of the project, separated according to its theoretical, experimental, and computational thrusts:

1.1 Theoretical Accomplishments

1.1.1 Analysis of the dependence of the spatial pBRDF distribution on the 3D shape

We developed a unified theoretical framework to analyze compressive sensing, sparse representation, and reconstruction of space objects in the combined spatial-spectral domain. The usual hyperspectral imaging approach gathers data over a full range of 2D spatial coordinates and 1D spectral channels in what is called a data cube. In most cases, such data typically carry relatively small amounts of information in a highly redundant manner, since space objects whether man-made (like satellites) or naturally produced (like asteroids and other space debris) are typically composed of a much smaller number of primitives, e.g., spatially and materially homogeneous elements and geometrically simple parts, than the number of voxels in the full data cube.

Theoretical work proceeded along two different lines. The first entailed constructing simple forward models for the SOI problem. This construction begins with a low-dimensional parametric model of space-object surfaces using a superquadric parameterization. Superquadrics are generalizations of ellipsiodal, hyperboloidal, and toroidal surfaces based on changing the powers of the Cartesian-to-spherical coordinate relationships for such ordinary 3D surfaces.

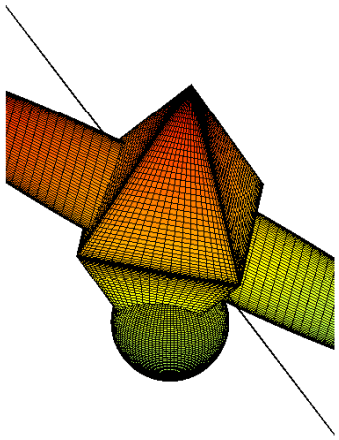

Figure 1: A satellite mock-up composed of five simple superquadrics

For example, a super-ellipsoid may be parameterized as follows:

$$\begin{aligned} x =& a_1 \cos^{\epsilon_1} \eta |\cos\omega|^{\epsilon_2} \mathrm{sgn}(\cos\omega); \\ y =& a_2 \cos^{\epsilon_1} \eta |\sin\omega|^{\epsilon_2} \mathrm{sgn}(\sin\omega); \\ z =& a_3 |\sin\eta|^{\epsilon_1} \mathrm{sgn}(\sin\eta), \end{aligned} \tag{1}$$

where the five parameters $a_1, a_2, a_3, \epsilon_1, \epsilon_2$ are chosen to be all positive. The first three determine the spatial scale of the three orthogonal dimensions in the object while the last two the geometrical shape of the solid. An example of a satellite mock-up composed of five different superellipsoids is shown in Fig. 1. By parameterizing the relatively small number of simple geoemtrical shapes that constitute a 3D satellite body via superquadrics, we can turn a complex surface characterization problem involving thousands of surface pixels into one involving a rather small number of parameters. These parameters can be estimated from a kinematic sequence of 2D images of such a 3D body, as we have shown previously for low-dimensional but non-superquadric parameterizations.

Once such a 3D space-object surface model is constructed, it may be ascribed material properties, specifically what material comprises what superquadric component of such a body. The surfaces are then given texture. To do so, we have modeled the surfaces of the individual superquadrics as being microscopically rough so they do not scatter sunlight simply via specular reflection. We have used a realistic roughness model for surfaces in 3D that may be described statistically by means of a distribution of planar micro-facets with varying surface-normal orientations relative to the underlying idealized microscopically smooth surface. Such surfaces, since they are typically made from dielectric materials, reflect and refract, so there is both a single-scattering specular component and a multiply-scattered diffuse Lambertian component. It is the latter component, which gives an opaque surface its spectral character, *i.e.,* color, in solar reflection. Both these components contribute to the spectral power density but only the specular albedo has a polarimetric content that

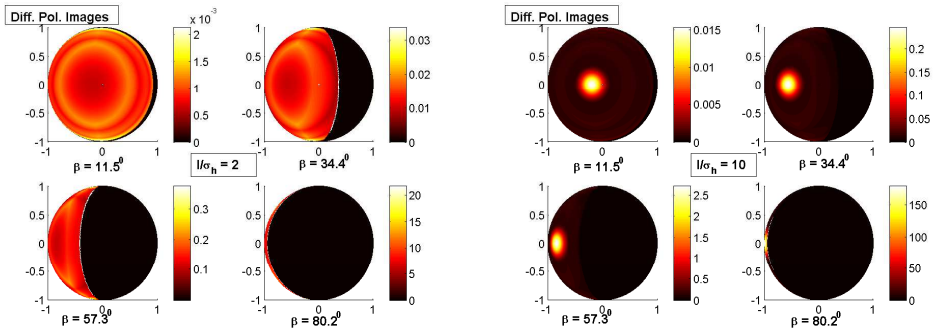

(a) (b)

Figure 2: The 2D spatial distribution of difference-polarization intensity in solar reflection from a sphere for four different solar angles for (a) smooth surface; (b) rough surface.

carries information about both the local shape and roughness of the space object. Thus, when supplemented with a sensor noise model, a model for atmospheric propagation and a blur model for the observing instrument, our calculations allow us to simulate the spectral and polarimetric content of any observations one might make of the solar albedo from a space object of varying local shape and roughness profile. It is this end-to-end forward model that we are now beginning to simulate to demonstrate the validity of our compressive spectral-polarimetric sensing and reconstruction approach.

The power spectral density (PSD) of the diffuse solar albedo depends only on the dispersion of the materials comprising the surface, rather than its shape or roughness, and has been extensively measured for a host of materials commonly present on a satellite. We therefore do not focus on the diffuse PSD in our effort, but analyze the specular albedo which, as we have noted, depends not just on material dispersion but also on the surface shape and roughness. We present some of our results of this analysis in Fig. 2 where we display the difference-polarization (H-V) images of a roughened sphere of Si at a specific wavelength and four different solar angles of illumination. It is clear that roughness, as measured by the ratio of the standard deviation of the heights of the microfacets and its length affects the footprint of the polarimetric signature of the surface. For highly smooth surfaces, the polarimetric difference image is limited to the glint spot, but as the surface becomes rougher, the spot containing polarimetric information spreads out in a way that is a measure of the roughness (for fixed shape), as we see in Fig. 2(b).

In Fig. 3, we plot the depedence of the angle-integrated power in the specular component as a function of the solar angle and varying roughness. As roughness increases, the specular component decreases in its fractional power when compared to the diffuse albedo, so the surface becomes more Lambertian and acquires its spectral signature that gives it a color and spectral content quite distinct from the white-light spectrum of the illuminating sunlight. By parameterizing the relatively small number of simple geoemtrical shapes and materials that constitute the space object and their roughness levels, represented by the ratio of the statistical scatter of microfacet heights to their lateral dimensions, we thus have an excellent forward model for varying local shapes, spectral reflectances, and roughness levels of a general space object.

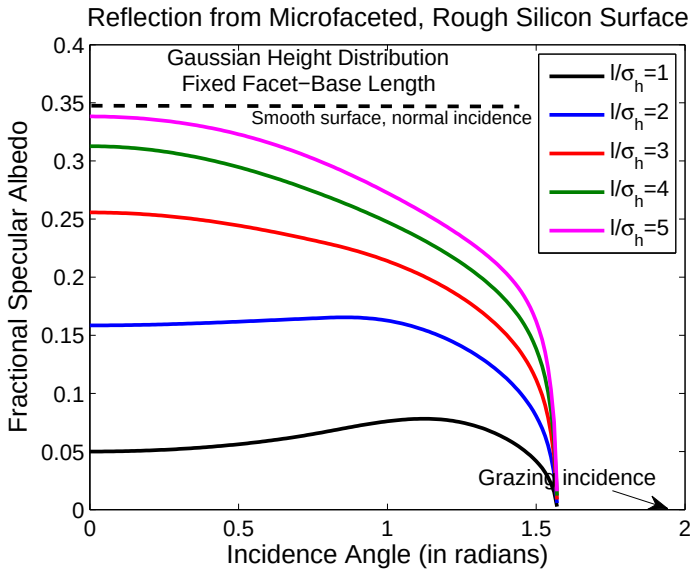

Figure 3: The total specular return fraction, sHDR, in solar reflection vs. the solar angle for different roughness levels

1.1.2 Extensions of the micro-facet-based roughness model to include hemispherical pits and proposal of a more general, composite roughness model

For ideally smooth, reflecting objects, the solar-reflected signal is rather uninteresting, characterized by simple glint points at which the condition for specular reflectance is met precisely. Such objects have furthermore spectral traces that closely reproduce the solar spectrum which they reflect rather faithfully, and thus appear white. But such idealized surfaces are just that, and in reality they undergo processes of weathering by solar wind and other particulate surface damage, e.g., from microdebris flying around, that roughen them. Roughening spreads the reflected radiance over the surface around the idealized fglint points in a way that depends crucially on the detailed surface shape in the vicinity of the glint points. Roughening can thus enable surface shape extraction if a detailed physical model can be derived that can predict such dependence on shape and roughness. Derivation of such a forward model has been a major emphasis of our theoretical work. We previously developed a micro-facet-based roughening model [5] in which the the strength of the polarimetric BRDF from any point on the object surface depends on its surface texture as well as the local shape and orientation relative to the observation direction via the spatial distribution of the reflected power around specularly refecting glint points.

We have recently extended the roughening model to include a statistical distribution of hemispherical pits, rather than - or even in addition to - microfacets, from which surface returns may be computed semi-analytically. These pits cause both included and excluded reflections since the curved surface of the pits allows solar light to be reflected in a whole range of directions not available to a smooth surface without pits, while the same curvedness also excludes points, those that lie in the shadow, from being operative in reflections along a corresponding range of directions. Such included and excluded reflections depend on the depth-to-radius ratio of the pit, and thus are statistically random for random but static

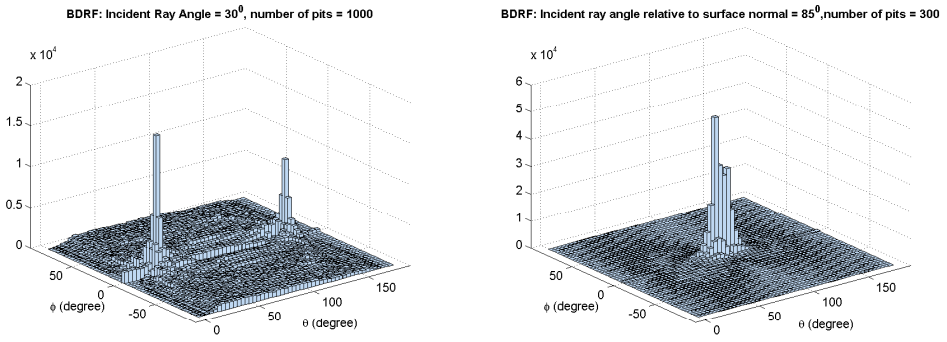

(a) (b)

Figure 4: The 2D angular histogram of reflected rays, including its specular and diffuse components, for solar reflection from a superquadric for two different solar incidence angles, 30^0 and 85^0, for a "pitted" rough surface with depth-to-radius ratio ranging uniformly between 0 and 1.

fluctuations of this ratio in a macroscopically small region of the surface. The nature of the reflected radiance, as captured by the distribution of allowed reflected ray directions, thius changes dramatically when compared to the micro-facet-based roughness model. This is shown in the following figure where the emergence of a two-peaked structure in the reflected-ray distribution - and thus in the BRDF - from a pit-based model is easily see, in sharp contrast with the previous model.

We can also separate out the specular, polarized part from the total polarimetric BRDF, so we can determine what fraction of the illumination power is returned in the unpolarized diffuse, Lambertian component. This requires determining the singly-reflected rays of all reflected rays, the former being those that leave the pit without encountering it again. This is a simple geometrical calculation we have recently completed. We are currently implementing this pit-based roughening model on curved surfaces to determine how for such surfaces the polarimetric BRDF, like in the micro-facet model, can potentially encode the 3D surface shape and surface texture.

We are using our two models of roughening to construct a composite roughness model that includes these two different roughness primitives - microfacets and hemispherical pits - occurring for a surface exposed to the two different mechanisms of roughening. The relative weight of the two BRDFs corresponding to the two mechanisms that contribute to the overall observable BRDF is a fitting parameter that can be extracted by solving the inverse problem of reconstruction and parameter recovery based on our forward roughening models. Indeed, this composite roughness model is easily extended further to include a whole variety of surface roughening and damage mechanisms with a set of probability weights to simulate realistically roughened surfaces in the space environment.

1.1.3 Developed a rotating PSF concept [6, 7, 8] to perform 3D imaging, being extended currently to include polarimetric imaging, in a single snapshot

The PI proposed and developed [6, 7, 8] a simple approach based on the use of a properly designed pupil phase profile that is divided into Fresnel-type zones, each with an integral number of complete phase windings that changes from one zone to the next by a fixed integer, to create a 3D point-spread function (PSF) that rotates with changing defocus, while keeping its transverse shape approximately invariant. This shape and size invariance of the rotating PSF can easily extend over ± 3-4 waves of defocus, with fairly compact dimensions that can provide excellent 3D precision for source localization and imaging of 3D shapes. Unlike Gauss-Laguerre mode-based approaches, it provides highly extended depth of field over a large transverse field of view to enable acquisition of large 3D volumes. The off-center spatial character of the rotating PSF allows it to resolve with ease sources that are in the same line of sight, which many other 3D imagers cannot typically do well. Further, it generalizes readily for encoding spherical aberration too via PSF rotation.

It can also be employed to effect 2D digital super-resolution (DSR) that overcomes the low-resolution iFOV limits of sensor data acquisition by collecting multiple image data frames that are different only in the axial defocus of their location. Current work in the PI's group is beginning to address the prospects of DSR by replacing the more traditional sub-pixel-shifts by changing axial defocus of PSF-rotated image frames.

The rotating-PSF approach can be extended by combining its spiral phase mask with a different kind of phase mask, called a q-plate, which is a birefringent phase plate with spiraling optical axis of phase retardation. Since the q-plate can convert right and left circular optical polarizations into $\pm q$ waves of orbital angular momentum, this combination mask enables one to generate different kinds of rotating PSFs for different source polarization states. In other words, we have a new approach to perform full 3D polarimetric imaging in a single snapshot. This promising concept, with tremendous implications for SSA and general space-based imaging and debris localization, has been proposed for further study under a currently pending proposal to AFOSR in the Imaging Science program headed by Dr. Julie Moses.

1.1.4 Asymptotics of Bayesian Error Probability and Source Super-Localization [9]

We carried out an asymptotic analysis of the minimum probability of error (MPE) in inferring the correct hypothesis in a Bayesian multi-hypothesis testing (MHT) formalism using many pixels of data that are corrupted by signal dependent shot noise, sensor read noise, and background illumination. We performed our analysis for a variety of combined noise and background statistics, including a pseudo-Gaussian distribution that can be employed to treat approximately the photon-counting statistics of signal and background as well as purely Gaussian sensor read-out noise and more general, exponentially peaked distributions. We subsequently evaluated both the exact and asymptotic MPE expressions for the problem of three-dimensional (3D) point source localization. We focused specifically on our recently proposed rotating-PSF imager and compared, using the MPE metric, its 3D localization performance with that of conventional and astigmatic imagers in the presence of background

and sensor-noise fluctuations.

Based on the powerful asymptotic error analysis, we determined that the rotating PSF imager has the best super-localization performance, of all 3D imagers considered here, over a large focal volume containing multiple point sources. This work was also presented at the 2014 International Quantitative Bio-Imaging workshop as a poster, and elicited much interest from the single-molecule bio-imaging community.

The analysis represents the achievement of an important theoretical milestone in error analysis of single-molecule localization that is not limited in applicability as are those based on the Fisher information and associated Cramer-Rao bound on the error of estimation.

1.1.5 Asymptotics of Bayesian Error Probability and 2D Pair Superresolution [10]

We applied the asymptotic Bayesian multi-hypothesis testing (MHT) based error analysis developed in the previous paper (see above) to treat the problem of superresolution imaging of a pair of closely spaced, equally bright point sources. The analysis exploits the notion of the minimum probability of error (MPE) in discriminating between two competing equiprobable hypotheses, a single point source of a certain brightness at the origin vs. a pair of point sources, each of half the brightness of the single source and located symmetrically about the origin, as the distance between the source pair is changed. For a Gaussian point-spread function (PSF), the analysis makes predictions on the scaling of the minimum source strength, expressed in units of photon number, required to disambiguate the pair as a function of their separation in both the signal-dominated and background-dominated regimes. Certain logarithmic corrections to the quartic scaling of the minimum source strength with respect to the degree of superresolution characterize the signal-dominated regime, while the scaling is purely quadratic in the background-dominated regime. For the Gaussian PSF, general results for arbitrary strengths of the signal, background, and sensor noise levels were also presented.

The applicability of this error analysis to more complicated imagers is being currently pursued. Our hope is to provide a comprehensive Bayesian inference based description and quantitative understanding of other imagers in performing 3D superresolution imaging of closely spaced point sources.

1.1.6 Bayesian Error Based Sequences of Statistical Information Bounds [11]

The relation between statistical information and Bayesian error has been sharpened by deriving finite sequences of upper and lower bounds on the equivocation entropy (EE) in terms of the minimum probability of error (MPE) and related Bayesian quantities. The well known Fano upper bound and Feder-Merhav lower bound on the EE are tightened by including a succession of posterior probabilities starting at the largest, which directly controls the MPE, and proceeding to successively lower ones. A number of other interesting results were also derived, including a sequence of upper bounds on the MPE in terms of a previously introduced sequence of generalized posterior distributions. The tightness of the various bounds was numerically evaluated for a simple example. These new bounds are not just computationally efficient but they are sufficiently simple to interpret analytically, and can thus

provide excellent framework in which to analyze information processing systems that use finite codewords for which some of the more powerful asymptotic approaches cannot be used without incurring large errors.

Our plan for current and future work is to employ some of these bounds to analyze fundamental upper limits of performance of 3D imaging systems like rotating-PSF imagers when only a few pixels of image data are available or practical, e.g., in the point-source localization scenario where many sources cover a relatively small image area so only a few pixels per source can be used to localize each source. An asymptotic analysis would not be sufficiently accurate in such a situation, but the bounds developed in this work can be used with much accuracy.

1.2 Experimental Accomplishments

1.2.1 Coded aperture snapshot spectral polarization imaging - early version using two birefringent crystals in combination with a single disperser and a grayscale coded mask

We demonstrated a coded aperture snapshot spectral polarization imager based on compressive sensing. In a snapshot, this system can calibrate the difference of the two linear orthogonal polarization states along with their spectral-spatial signature with large field of view. A grayscale 2D detector array is utilized to record the coded mixture of spatial, spectral and polarization information of the object. In the end, a fast imaging reconstruction algorithm called TwIST is utilized to reconstruct the polarized spectral image.

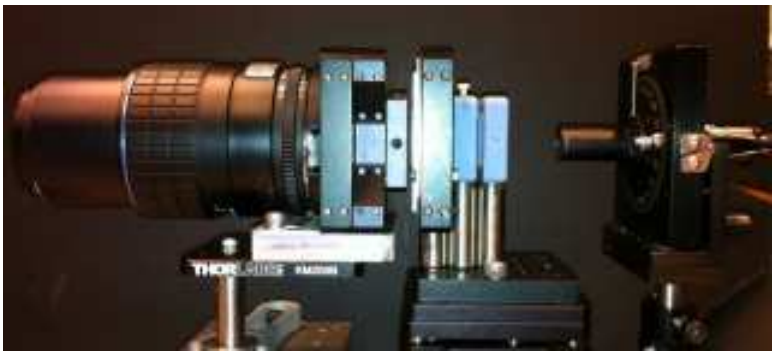

Figure 5: System setup.

Figure 5 is a photograph of the experimental prototype. The objective lens in this setup is a commercialized objective form Jenoptik (Easthampton, Massachusetts). The coded aperture is a lithography patterned on a quartz substrate with an anti-reflection coating on both sides, with 1988*1988 elements random binary pattern that are each 7.4 μm square. The birefringent material are two calcite crystals which manufactured by United Crystals (Port Washington, New York), with 8mm thickness, 2.5 cm square clear aperture and 45^o optical axis angle relative to the light propagation axis. The magnification of the relay lens is 0.38. Finally, the detector is an 8-bit monochrome CMOS camera form Aptina (San Jose, California) with 4384*3288 pixels that are each 1.4 μm square. All of these system components are aligned on a mounting plate. The detector and the objective lens are

carried by translation stages in order to provide the ability to adjust the focusing distance. The detector was placed on a rotation mount to ensure the proper alignment of the beams dispersion direction across the image plane.

Figure 6 represents the design and the dispersion relation of the birefringent crystal pair. The optical axes of the first and the second calcite plates orientate 45^o relative to the y-z plane and x-z plane, respectively. Therefore, the ordinary ray (o-ray) of the first birefringent plate will become the extraordinary ray (e-ray) of the second plate and be shifted parallel to its original propagation direction. This image displacing effect split two orthogonal polarized images. In addition, the displacing distance follows the refraction law, which results in image sharing at wavelength dependent location. When the images pass through the crystal pair, those birefringent crystals can generate the polarization selective image displacement and wavelength dependent image dispersion. Both modulations are due to the double refraction effect of the calcite crystals.

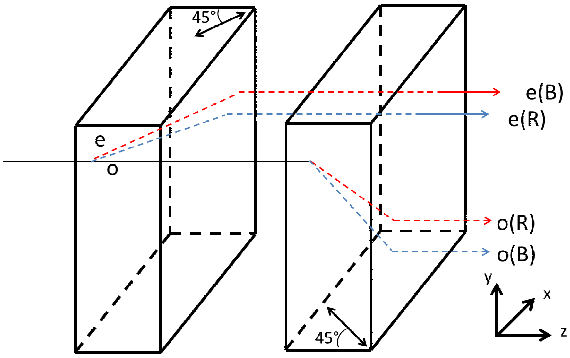

Figure 6: Design of the birefringent crystals.

On the detector plane, the measurement in this system is a two-dimensional projection of two separated three-dimensional spatial-spectral data cube which include the information form the scene. The data reconstruction form this compressive sensing based on assuming the object has the sparsity in some basis, which making the object highly compressible. Here the reconstructing process relies on the two-step iterative shrinkage and thresholding (TwIST) algorithm. We also assume the piecewise smoothness of object in spatial domain and the sparsity in the wavelet basis is enforced by utilizing the total variation regularization.

To test the performance of the system and the reconstruction algorithm, we measured negative 1951 USAF resolution test chart to validate the ability of the TwIST algorithm to estimate the variation in spectral signature and partial polarization state distribution in an image. The test chart was illuminated by a Tungsten light bulb and filtered by a linear polarizer. The light was guided by a multimode fiber and collimated by a commercialize beam expander. A linear polarizer was placed after the collimator to control the incident polarization state of the system. The transmission image of the test chart was modulated and then acquired by the measurement system. Figure 7 shows a detector measurement of the test chart. The dispersion and splittering which was generated by the two birefringent crystals redistributed the intensity of the incident image. As shown in the figure, the measurement on the detector plane is the superposition of the two overlapping images; each image is

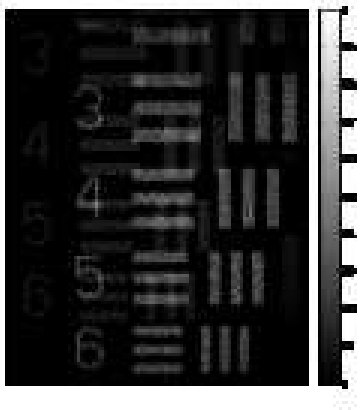

Figure 7: Detector measurement.

modulated by the coded pattern. A 400-680 nm band-pass filter was mounted in front of the objective lens to confine the measurement of the scene within the corresponding wavelength channels.

Figure 8 presents the reconstruction of 19 wavelength channel and two Stokes vectors between 400 and 680 nm. The left part of the reconstruction shows the S_0 term of the scene, which is total irradiance of the object; the right part shows the S_1 term, which represents the polarization difference in intensity. The spatial modulation pattern and the image overlapping in Figure 5 had been removed and clear resolution charts with sharp edge had been reconstructed by the TwIST algorithm in majority of the wavelength channels. The brightness in the reconstructed figure represents the relatively intensity between the wavelength channels. Since the azimuth angle of the incident polarizer was 30^o relative to the plane of the optical table, the ideal value of the S_1 terms is 0.5. Based on the result in Figure 4, the brightness of the images in all S_1 channels are around half of value as the corresponding irradiance channels, which fits the theoretical value.

To test the performance of the spectral reconstruction, we compared the reconstructed spectral signature of the test chart and the reference spectrum was acquired using a commercial Ocean Optics USB2000 spectrometer. For comparison, the continuous reference spectrum was integrated into the 19 spectral bands based on the channel width of this system. Figure 9 shows the reconstructed spectrum of the test chart in blue star and the reference spectrum in red line. Both spectrums were normalized to the maximum value in their curves. The reconstructed spectrum represents the spectral distribution of the average intensity within a selected area in the test chart. The comparison demonstrates the agreement between the reconstructed and the reference spectrum, indicating that the reconstruction can correctly identify the spectral data.

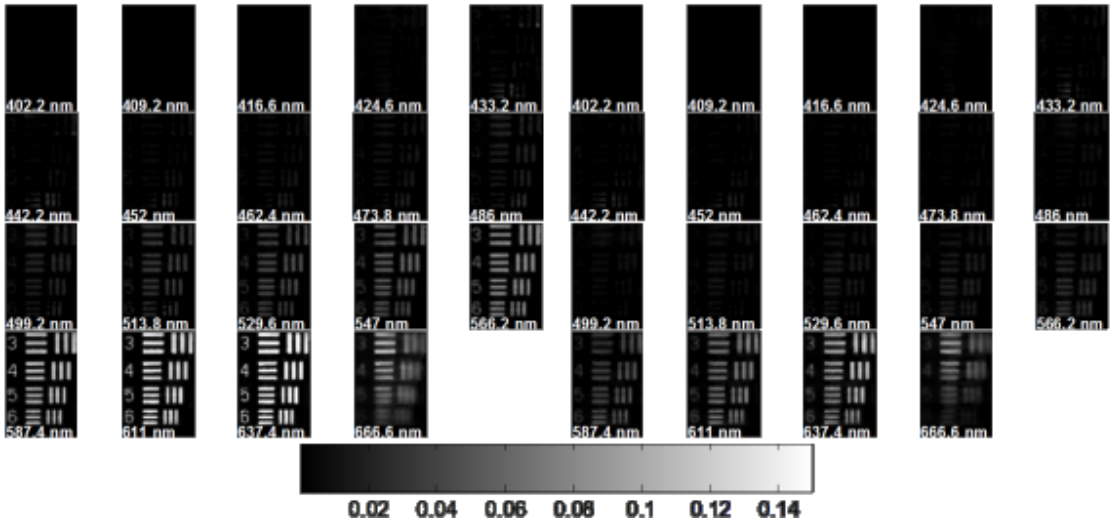

Figure 8: Reconstruction result of a negative 1951 USAF resolution test chart.

1.2.2 Coded aperture snapshot spectral polarization imaging - improved version using coded aperture, polarizers, and LC-SLM to create joint polarization and spectral encoding

We next employed a vastly improved design based on the use of a liquid crystal on silicon modulator to jointly code spatial, spectral and polarization features for snapshot spectral imaging. We demonstrate compressive sampling of megapixel multispectral image on a two-dimensional (2D) detector array. The reconstruction recovers the encoded 2D measurement to a 4D data cube The 4D data cube includes megapixels in spatial domain, 15 wavelength channels between 450 and 680 nm and their horizontal and vertical polarized irradiance.

A schematic of this SLM based CASSI system is shown in Fig. 10. An objective lens L1 images the scene from a remote distance, and the lenses L2, L3 relay the scene through the beam splitter and the wave plate onto the modulator. The SLM modulates the scene with spatially distributed polarization state rotation and then reflects the image back. The SLM generated degree of polarization state rotation is a wavelength dependent value. The imaging lenses L3 and L4 relay the modulated image onto the detector plane through the polarizer. To achieve best contrast in every wavelength, we insert an achromatic quarter wave-plate in the light path in order to compensate the extra phase retardation in the liquid crystal device. Finally, the detector array records modulated patterns in every wavelength, which involves the spectral and spectral, and polarization modulated information of the object.

Fig. 11 is a photograph of the experimental setup. The setup includes a 60 mm objective lens (Jenoptik), one 70 mm achromatic lens (Newport), a dichroic beam splitter (Newport), an achromatic quarter wave plate, a liquid crystal based SLM (Pluto, Holoeye), two 25 mm imaging lenses (Computar), a sheet polarizer(CVI) ,and a monochrome CCD camera (Pike F-421, AVT) with 2048 x 2048 pixels that are 7.4 μm square. A band pass filter (Badder) is mounted on the objective lens to cut the ultra-violet and infrared. The transmission of the filter, the reflection of the SLM and the quantum efficiency of the detector limit the wavelengths of interest of this system between 450 nm and 680 nm. The scattered image of

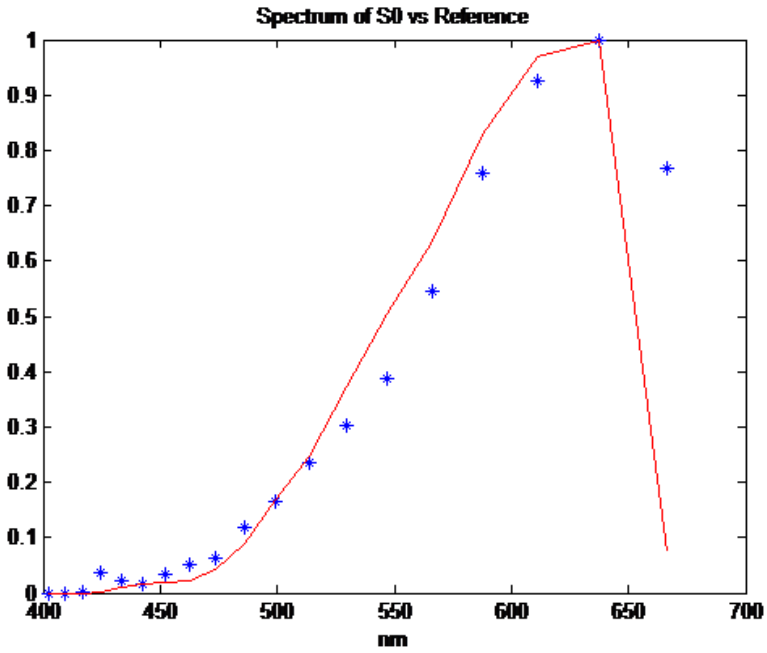

Figure 9: Comparison between the reconstructed and the reference spectrum.

the scene is first collected by the objective lens then projected on the SLM. After modulated by the SLM with transmission patterns, the scene is reflected and then propagated to the color insensitive detector.

The SLM plays an important role in this system because this revised design of polarization spectral imager replaces both the coding device and the dispersive element by this single modulator. This modulator is based on a reflective Liquid Crystal on Silicon (LCoS) microdisplay technique, which has a 1920x1080 pixels active area with 8 μm pixel pitch. Being down magnified by two imaging lenses, the width of each pixel on the SLM becomes 7.4 μm square. Considering a perfect alignment, it is possible to map each detector pixel with one corresponding pixels on the SLM. Each pixel on the microdisplay can be independently addressed by an 8-bit voltage value to change the amount of phase retardation to the incident polarized light. After propagating back through the polarizer splitter, the amount of retardation for two orthogonal polarized incident becomes different transmission to every voxel in the image data cube corresponding to its spatial voltage address and wavelength. This characteristic will be utilized to encode the image in spatial and spectral domains.

Here we used a random 8-bit (0-255) gray scale voltage code on the SLM to generate a group of different transmission patterns for each wavelength slice (450 to 680 nm) in the image data cube. The voltage address varies from 0 to 255, which represents 0 to 3 π phase delay at 630 nm. The transmission to voltage address and wavelength can be estimated by calibrating the SLM. The calibration process records the transmission under the two orthogonally polarized monochromatic illuminations and homogeneously applied voltage on the modulator. It also includes the transmission of all the optics, the quantum efficiency of the detector, and the phase modulation of the SLM. We averaged the transmission across the center area of the SLM and calculate its amplitude modulation, which is shown in Fig. 12.

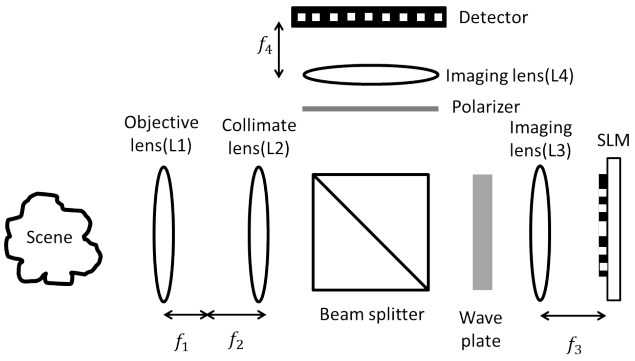

Figure 10: The system schematic. L1 is the objective lens images the scene. L2 and L3 relay the image onto the SLM. L3 and L4 project the encoded image on the detector. The polarizer is used to achieve intensity modulation mode of the SLM. The quarter wave plate compensates phase retardation of the SLM to achieve best contrast.

Based on the calibration, within 450 nm and 680 nm, an 8-bit voltage variation on the SLM generates a gray scale transmission ratio between 0.08 and 0.96.

Here the liquid crystal SLM generates joint wavelength and polarization dependent modulation for each spectral plane of the scene. The modulated spectral slices are integrated by a 2D detector, but the spectral information in the 4D data cube can be distinguished based on the corresponding transmission patterns between all wavelength channels.

1.2.3 A Further Improved Version of the SLM-CASSPI Instrument with Full Linear Polarimetric Coding

We decompose the compressed signal into 0^o, 90^o, 45^o, and 135^o polarization channels for linear polarization state estimation. This linear polarimetry would satisfy several applications without significant circular polarizations, such as most of the natural scenes.

The LC cell has a property of electrical controllable optical anisotropy, which enables the signal modulation for this camera. The long axis and the short axis of each layer of the LC cell provide different refractive indices to the incident wave. By controlling the orientation of the LC cell through tuning the applied voltage, the SLM can be considered as a variable wave-plate. We sampled the vertical fraction of the irradiance to transfer the phase modulation, given by β, into a detector recognizable amplitude modulation, which can be described as

$$I = (1/2)[S_0 - S_1 \cos(2\beta) + S_2 \sin(2\beta)],$$

in terms of the first three Stokes parameters, S_0, S_1, S_2.

Fig. 14 shows the amplitude modulation provided by the different polarization and color channels. Each sub-figure describes the relationship between the transmission pixel counts and the applied voltage on the SLM. We note that this camera has freedom of choosing the basis of polarization state decomposition. Here we use linear horizontal, linear vertical, linear 45, and linear 135 as the decomposing basis to analyze all linear polarization states.

Fig. 11 shows the experimental prototype of the compressive camera. A series of lenses projects the scene on the SLM, which is the intermediate image plane. A random voltage

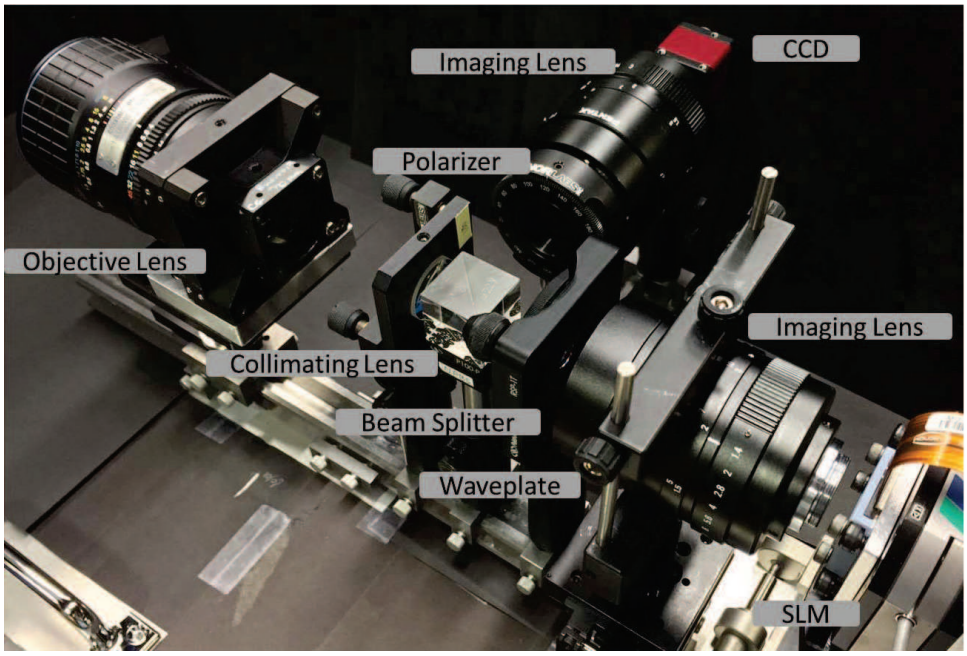

Figure 11: The experimental prototype of the system.

pattern is applied on the SLM, which provides a spectral and polarization dependent amplitude modulation to encode the object. After reflected by the silicon layer of the SLM and then filtered by the polarizer, the applied phase retardation becomes a wavelength and polarization dependent amplitude modulation which is added to the scene. We apply a quarter wave-plate as a compensator to increase the contrast ratio of the coding. The modulated image will then recorded by the color detector. Based on the design, this camera has a 25 field of view and a 12.5 mm clear aperture. The detector has a 1280x720 spatial resolution with 4.08um square pixel size. The modulation process can be represented by the following mathematical model:

$$g_{mn} = \int\int\int [f_{\parallel}(x,y,\lambda)T_{\parallel}(x,y,\lambda)+f_{\perp}(x,y,\lambda)T_{\perp}(x,y,\lambda)]\,\mathrm{rect}\,(x/\Delta-m, y/\Delta-n)dxdyd\lambda+w_{mn},$$

where g represents the power spectral density in the detector plane, f the spatial-spectral distribution of the scene, and $T_{\perp}$ and $T_{\parallel}$ are the wavelength and polarization dependent transmission code patterns. We note that the size of the detector pixel is Δ and its corresponding pixel noise is denoted by w. We depict the 4D discrete sampling function in matrix form as $\mathbf{g} = \mathbf{Hf} + \mathbf{w}$, where $\mathbf{H}$ represents the forward matrix of the system, $\mathbf{f}$ the vectorized and discretized object datacube, and $\mathbf{w}$ represents the sensor noise vector. The $\mathbf{H}$ matrix approximates the sampling, encodes the color and polarization channels to compress the 4D color and polarization datastream $\mathbf{f}$ on measurement $\mathbf{g}$. We experimentally calibrate the forward matrix $\mathbf{H}$ by illuminating the camera under four identical polarization states. We assign linear horizontal, linear vertical, linear 45^o, and linear 135^o polarization channels as the identical states. The light source we use is a white light LED filtered by a rotatable polarizer. We record the modulation patterns of these four polarizations sequentially. This calibration considers the errors which might break the ideal mapping relationship, such as

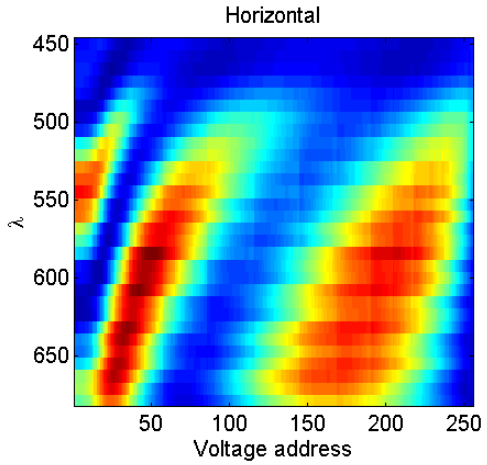

Figure 12: The intensity modulation of the SLM for horizontal polarized light. Given different voltages and incident wavelengths, the SLM combined with the optics generates corresponding transmission code.

the aberration of the optics and the sub-pixel misalignment.

Figs. 15 and 16 show the experimental result of the compressive camera. The objects are polarization filtered color bricks and a scene of a parking lot. Both of them include the spatial, spectral and polarization complexity. Both scenes are reconstructed by Two-step Iterative Shrinkage Thresholding (TwIST) algorithm combined with total variation (TV) regularization function. The reconstruction shows the linear horizontal, linear vertical, linear 45^o, and/or linear 135^o polarization channels with red, green, and blue color channels.

This single-shot compressive color polarization imager presents an integration of color and polarization compression. Such camera uniquely encodes and decomposes the scene into color polarization images through the phase modulation of a SLM along without any dispersive element. This technique eliminates mechanical movements that hinder conventional polarimetry. The experimental results show clear spatial resolution and low noise reconstructions in the experiments. Future applications will use the polarization sensitivity to analyze the surface information, such as the curvature and the roughness.

A similar setup can be used in compressive spectral imaging. Based on the singular value decomposition, this SLM modulation provides six measurement modes in spectral multiplexing. Therefore, it can effectively multiplex a spectrum which has up to six major spectral bands/peaks in the sensing region (400 to 680 nm) without losing information. This criterion can satisfy most of the spectral distribution of the natural scenes, which have smooth spectrum and only require two to three modes to fully represent their major distribution in the spectral domain. The minor detail can be recovered by the spectral constraint of the reconstruction algorithm, such as interpolating the relative spectral density to correct the reconstruction.

Here we use an SLM to encode the 3D spatial-spectral information on a 2D gray-scale detector - a similar CDMA strategy to CASSI for snapshot hyperspectral imaging. The SLM provides wavelength-dependent transmission patterns to multiplex every spectral channel for the compressive measurement. The hyperspectral slices can be separated by using inversion

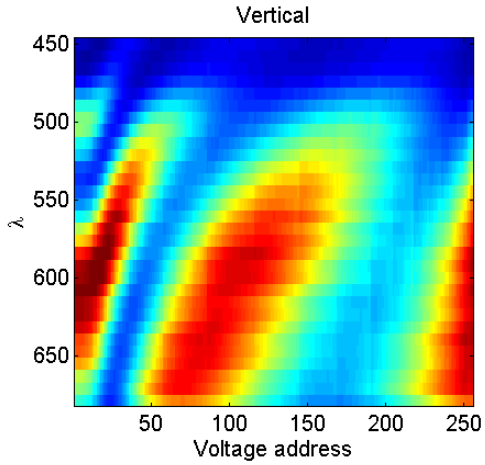

Figure 13: The intensity modulation of the SLM for vertical polarized light. Given different voltages and incident wavelengths, the SLM combined with the optics generates corresponding transmission code.

algorithms. We calibrated the spectral channels under a 5 nm spectral bandwidth by using a monochromator (iHR320, Horiba).

Figs. 17 and 18 show the preliminary reconstruction results of this compressive hyperspectral camera. The objects are color candies which are illuminated by a tungsten light source.

1.3 Computational Accomplishments

1.3.1 Randomized Singular-Valued Decomposition (SVD) Methods in Hyperspectral Imaging [12]

We advanced and tested a randomized singular value decomposition (rSVD) method for the purposes of lossless compression, reconstruction, classification, and target de- tection with hyperspectral (HSI) data. Recent work in low-rank matrix approximations obtained from random projections suggest that these approximations are well-suited for randomized dimensionality reduction. Approximation errors for the rSVD were eval- uated on HSI and comparisons were made to deterministic techniques and as well as to other randomized low-rank matrix approximation methods involving compressive prin- cipal component analysis. Numerical tests on real HSI data suggested that the method is promising, and is particularly effective for HSI data interrogation.

1.3.2 Deblurring and Sparse Unmixing For Hyperspectral Images [14]

We developed a new approach to joint deblurring and sparse unmixing of hyperspectral images based on a total variation regularization method:

$$\min_{X \geq 0} \quad \tfrac{1}{2} \left\| HXA - Y \right\|_F^2 + \mu_1 \left\| X \right\|_{1,1} + \mu_2 \mathrm{TV}(X)$$

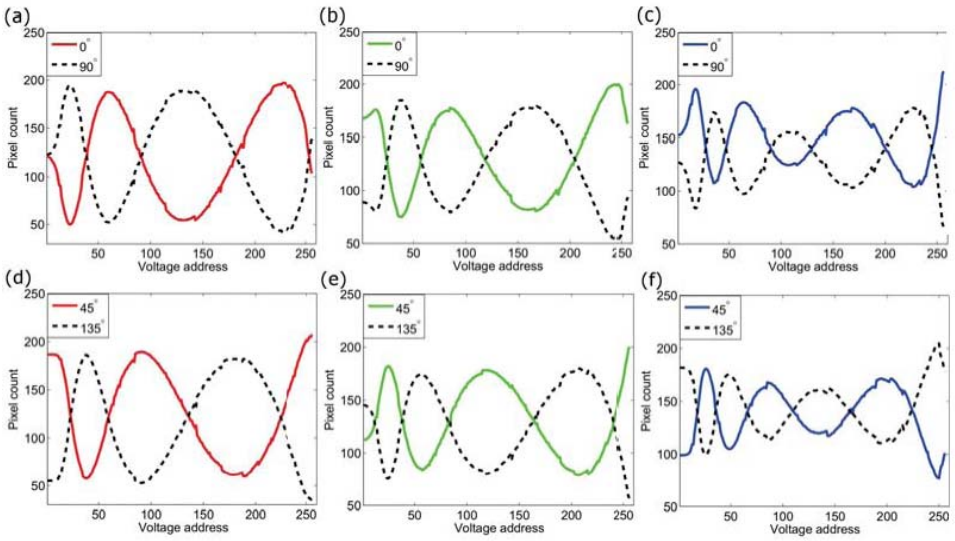

Figure 14: The amplitude modulation tests for three color channels and four polarization channels. The horizontal axis represents the 8-bit applied voltage address on the SLM. The vertical axis is the average pixel count.

where H is an n-by-n hyperspectral data acquisition blurring matrix, and μ_1 and μ_2 are two positive regularization parameters used to control the importance of the sparsity term and the total variation term, respectively. Here

$$\|X\|_{1,1} := \sum_{i=1}^{n}\sum_{j=1}^{m}|X_{i,j}|.$$

In the model we incorporated blurring operators for dealing with blurring effects accross the spectral bands, and in particular, blurring operators for hyperspectral imaging whose PSFs are generally system dependent and result from axial optical aberrations in the acquisition system. An alternating direction method was developed to solve the resulting optimization problem efficiently. According to the structure of the total variation regularization and sparse unmixing in the model, the convergence of the alternating direction method can be guaranteed. Experimental results were reported to demonstrate the effectiveness of the TV and sparsity model and the efficiency of the proposed numerical scheme, and the method was compared to the recent Sparse Unmixing via variable Splitting Augmented Lagrangian and Total Variation (SUnSAL-TV) method by Iordache, Bioucas-Dias, and Plaza.

Here we assumed that the PSF leading to the blurring matrix for hyperspectral data has already been estimated. As discussed above, hyperspectral image degradation is often "system dependent," and the point-spread function (PSF) of the image acquisition system needs to be identified. The system PSF relates generally to axial optical aberrations, while spatial PSFs relate to the usual image blurring problems such as defocus, motion, imaging through a medium, etc. Axial optical aberrations can lead to a significant blurring of image intensities in certain parts of the spectral range. These axial optical aberrations arise from the index of refraction variations that is dependent on the wavelength of incident light. In a recent paper by Spiclin, et al., the authors assumed a model of the PSF to be a "linear

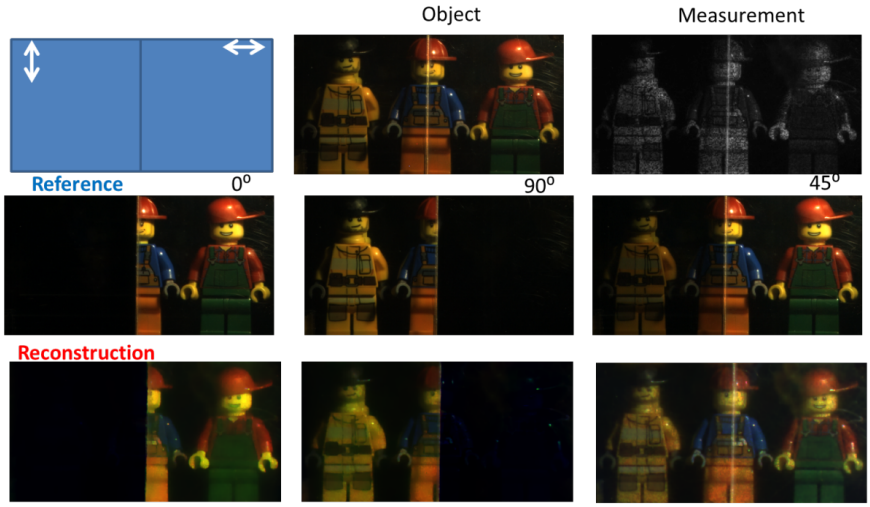

Figure 15: The measurement, the references, and the reconstruction of toys which is filtered by two orthogonal sheet polarizers. The upper left shows the azimuth angle of the polarizer. The upper middle and upper right show the irradiance of the object and the raw measurement of the compressive polarization camera, respectively. The second row shows the reference images measured by a camera filtered by a rotatable polarizer. The third row shows the pseudo-color reconstruction.

combination of Gaussian functions" across the different spectral bands, therefore the overall PSF blur identification process is reduced to finding only the corresponding scalar weight for each Gaussian function.

1.3.3 Sparse Nonnegative Matrix Underapproximation and its Application to Hyperspectral Image Analysis [15]

Dimensionality reduction techniques such as principal component analysis (PCA) are powerful tools for the analysis of high-dimensional data. In hyperspectral image analysis, nonnegativity of the data can be taken into account, leading to an additive linear model called nonnegative matrix factorization (NMF), which improves interpretability of the decomposition. Recently, another technique based on underapproximations (NMU) has been introduced, which allows the extraction of features in a recursive way, such as PCA, but preserving nonnegativity, such as NMF. Moreover, in some situations, NMU is able to detect automatically the materials present in the scene being imaged. However, for difficult hyperspectral datasets, NMU can mix some materials together, and is therefore not able to separate all of them properly. In this paper we introduce sparse NMU by adding a sparsity constraint on the abundance matrix and use it to extract materials individually in a more efficient way than NMU. This was experimentally demonstrated on the HYDICE images of the San Diego airport and the Urban dataset.

Figure 16: The measurement, the references, and the reconstruction of a scene of a parking lot. The upper left and upper right show the irradiance of the object and the raw measurement of the compressive polarization camera, respectively. The second row shows the reference images measured by a camera filtered by a rotatable polarizer. The third row shows the pseudo-color reconstruction. Notice that the reflections on the windows and on the rear screen of cars are polarized.

1.3.4 Randomized Methods in Lossless Compression of Hyperspectral Data [16]

We evaluated recently developed randomized matrix decomposition methods for fast lossless compression and reconstruction of hyperspectral imaging (HSI) data. The simple random projection methods have been shown to be effective for lossy compression without severely affecting the performance of object identification and classification. We built upon these methods to develop a new double-random projection method that may enable security in data transmission of compressed data. For HSI data, the distribution of elements in the resulting residual matrix, i.e., the original data subtracted by its low-rank representation, exhibits a low entropy relative to the original data that favors high-compression ratio. We showed both theoretically and empirically that randomized methods combined with residual-coding algorithms can lead to effective lossless compression of HSI data. We conducted numerical tests on real large-scale HSI data that shows promise in this case. In addition, we showed that randomized techniques can be applicable for encoding on resource-constrained on-board sensor systems, where the core matrix-vector multiplications can be easily implemented on computing platforms such as graphic processing units or field-programmable gate arrays.

1.3.5 Joint Blind Deconvolution and Spectral Unmixing of Hyperspectral Images [17]

Our interest here was spectral imaging for space object identification based upon imaging using simultaneous measurements at different wavelengths. AMOS sensors can collect simultaneous images ranging from visible to LWIR. On the other hand, multiframe blind

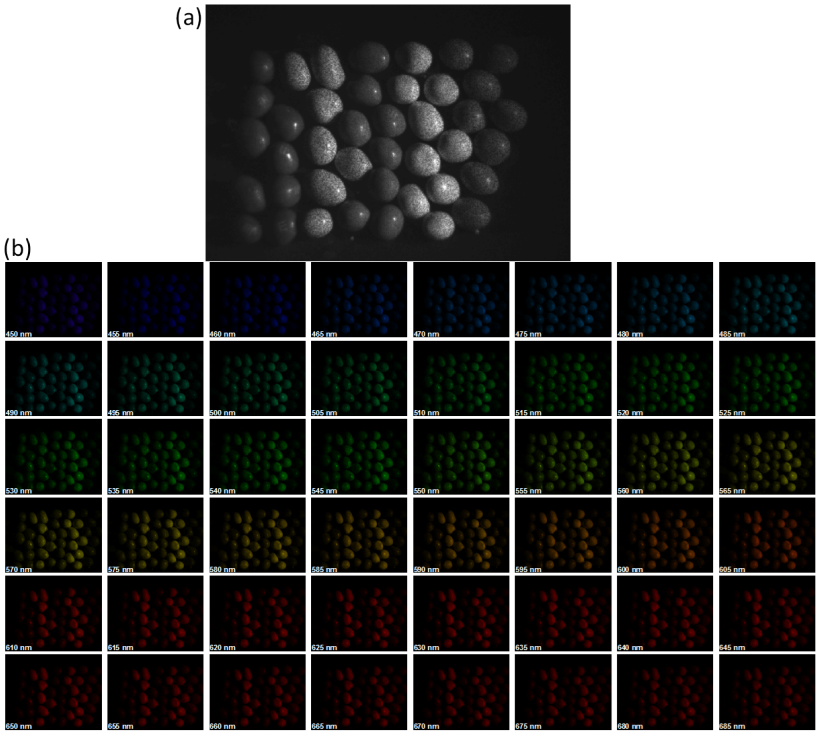

Figure 17: The reconstruction of compressive hyperspectral camera. (a) The raw measurement of the color candies. (b) The 48 spectral channels reconstruction between 450nm and 685 nm.

deconvolution (MFBD) has demonstrated success by acquiring near-simultaneous multiple images for reconstructing space objects, and another success has been shown through adding phase diversity (PD) by splitting the light beam in channels with different phase functions. So far, most MFBD and PD applications have been focused on monochromatic images, with a few MFBD studies on multispectral images, also called the wavelength diversity. In particular, B. Calef has shown that wavelength-diverse MFBD is a promising technique for combining data from multiple sensors to yield a higher-quality reconstructed image. Here, we presented optimization algorithms to blindly deconvolve observed blurred and noisy hyperspectral images with phase diversity at each wavelength channel. We used the facts that at longer wavelengths, turbulence effects on the phase are less severe, while diffraction effects at shorter wavelengths are less severe. Moreover, because the blurring kernels of all wavelength channels essentially share the same optimal path difference (OPD) function, we have greatly reduced the number of parameters in the blurring kernel. We modeled the true hyperspectral object by a linear spectral unmixing model, which reduces the number of pixels to be recovered. Because the number of known parameters is far greater than the number of unknowns, the method enjoys an enhanced capability of successful reconstruction. We simultaneously reconstructed the true object, estimated the blurring kernels, and separate the object into spectrally homogeneous segments, each characterized by its support and spectral signature,

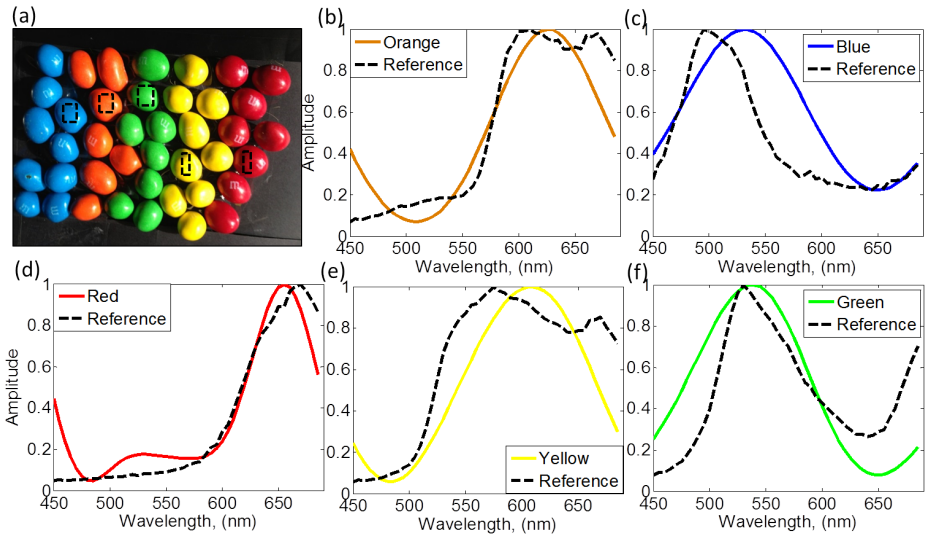

Figure 18: The spectral reconstruction of color candies. (a) The reference image measured by a color camera. (b) to (f) are the averaged reconstruction spectra of orange, blue, red, yellow and green candies, respectively. The reference spectra are measured by a fiber spectrometer.

an important step for analyzing the material compositions of space objects.

1.3.6 Shape and Pose Recovery of Solar-Illuminated Surfaces from Compressive Spectral-Polarimetric Image Data [5]

We performed simulation-based studies of the use of compressively sensed spectral polarimetric spatial image data from a solar illuminated reflecting surface to recover its material signature, three-dimensional (3D) shape, pose, and degree of surface roughness. The spatial variations of the polarimetric BRDF around glint points contain unique information about the shape and roughness of the reflecting surface that is revealed most dramatically in polarization-difference maps from which the spatially generalized diffuse-scattering contributions to brightness are largely absent. Here we employed a specific compressed-sensing protocol, the so-called Coded-Aperture Snapshot Spectral Polarimetric Imager advanced recently by Tsai and Brady under partial support from this grant and discussed in detail in Section 1.2 of this report, to simulate noisy measurements from which these surface attributes are recovered in a sequential manner. Even in the presence of additive sensor noise, the recovery of these surface attributes seemed to be quite robust.

1.3.7 Image Reconstruction from Double Random Projection [18]

We advanced double random projection methods for reconstruction of imaging data. The methods draw upon recent results in the random projection literature, particularly on lowrank matrix approximations, and the reconstruction algorithm has only two simple and non-iterative steps, while the reconstruction error is close to the error of the optimal low-rank approximation by the truncated singular-value decomposition. We extended the often-required symmetric distributions of entries in a random-projection matrix to asymmetric

distributions, which can be more easily implementable on imaging devices. Experimental results were provided on the subsampling of natural images and hyperspectral images, and on simulated compressible matrices. Comparisons with other random projection methods were also provided.

1.3.8 Deblurring and Sparse Unmixing of Hyperspectral Images using Multiple Point Spread Functions [19]

We advanced an iterative approach to solve separable nonlinear least squares problems arising in the estimation of wavelength-dependent point spread function (PSF) parameters for hyperspectral imaging. A variable projection Gauss-Newton method was used to solve the nonlinear least squares problem. An analysis shows that the Jacobian can be potentially very ill-conditioned. To deal with this ill-conditioning, we used a combination of subset selection and other regularization techniques. Experimental results related to hyperspectral PSF parameter identification and star spectrum reconstruction illustrate the effectiveness of the resulting numerical scheme.

1.3.9 Estimation of Atmospheric PSF Parameters for Hyperspectral Imaging [20]

A numerical approach was provided for deblurring and sparse unmixing of ground-based hyperspectral images (HSI) of objects taken through atmospheric turbulence. Hyperspectral imaging systems capture a 3D datacube (tensor) containing: 2D spatial information, and 1D spectral information at each spatial location. Pixel intensities vary with wavelength bands providing a spectral trace of intensity values, and generating a spatial map of spectral variation (spectral signatures of materials). The deblurring and spectral unmixing problem is quite challenging since the point spread function (PSF) depends on the imaging system as well as the seeing conditions and is wavelength varying. We showed how to efficiently construct an optimal Kronecker product-based preconditioner, and provide numerical methods for estimating the multiple PSFs using spectral data from an isolated (guide) star for joint deblurring and sparse unmixing the HSI datasets in order to spectrally analyze the image objects. The methods were illustrated with numerical experiments on a commonly used test example, a simulated HSI of the Hubble Space Telescope satellite.

2 Publications Supported by the Project during the Period of Performance

The following manuscripts have resulted in part from the funding support derived from the grant:

[1] S. Prasad, "New Error Bounds for M-Testing and Estimation of Source Location with Sub-Pixel Precision," J. Opt. Soc. Am. A **29**, 354-366 (2012).

[2] S. Prasad and S. Narravula, "Applications of Shannon information and statistical estimation theory to inverse problems in imaging," *Signal Recovery and Synthesis* Topical

Meeting of the Optical Society of America, Toronto, CA (July 11, 2011). Abstract available at http://www.opticsinfobase.org/abstract.cfm?URI=SRS-2011-SMC1

[3] S. Prasad, Q. Zhang, R. Plemmons, and D. Brady, "Statistical performance bounds for coded-aperture compressive spectral-polarimetric imaging," *Computational Optical Sensing and Imaging (COSI)* Topical Meeting of the Optical Society of America, Monterey, CA (24-27 June 2012). Abstract available at http://www.opticsinfobase.org/abstract.cfm?URI=COSI-2012-CTu3B.1

[4] Kittle, D., Zhang, Q., Plemmons, R.J., Brady, D., and Prasad, S., "Joint Segmentation and Reconstruction of Coded Aperture Hyperspectral Data," *Computational Optical Sensing and Imaging (COSI)* Topical Meeting of the Optical Society of America, Toronto, Canada (July 2011). Abstract available at http://www.opticsinfobase.org/abstract.cfm?URI=COSI-2011-CMD1

[5] S. Prasad, Q. Zhang, and R. Plemmons, "Shape, Pose, and Material Recovery of Solar-Illuminated Surfaces from Compressive Spectral-Polarimetric Image Data," Proceedings of the 2013 AMOS Technical Conference,Maui, HI, Sep 10-13, 2013. Available (8 pages) at http://www.amostech.com/TechnicalPapers/2013.cfm

[6] S. Prasad, "Rotating Point Spread Function by Pupil Phase Engineering," Opt. Lett. **38**, Iss. 4, pp. 585-587 (2013).

[7] Rakesh Kumar and S. Prasad, "PSF Rotation with Changing Defocus and Applications to 3D Imaging for Space Situational Awareness," Proceedings of the 2013 AMOS Technical Conference,Maui, HI, Sep 10-13, 2013. Paper (9 pages) available at http://www.amostech.com/TechnicalPapers/2013.cfm

[8] S. Prasad, Rakesh Kumar, and S. Narravula, "Angular Momentum, Rotating PSF, and 3D Source Localization," *Computational Optical Sensing and Imaging (COSI)* Topical Meeting of the Optical Society of America, Kona, HI (24-26 June 2014). Abstract available at http://www.opticsinfobase.org/abstract.cfm?URI=COSI-2014-CTh2C.1

[9] S. Prasad, "Asymptotics of Bayesian Error Probability and Source Super-Localization in Three Dimensions," Opt. Express, Vol. 22 Issue 13, pp.16008-16028 (2014).

[10] S. Prasad, "Asymptotics of Bayesian Error Probability and 2D Pair Superresolution," Opt. Express, Vol. 22 Issue 13, pp.16029-16047 (2014).

[11] S. Prasad, "Bayesian error based sequences of mutual information bounds," to appear in IEEE Trans. Inform. Th. (2015).

[12] J. Zhang, J. Erway, X. Hu, Q. Zhang, and R. Plemmons, "Randomized SVD Methods in Hyperspectral Imaging," J. Electrical and Computer Engineering, Special Issue on Spectral Imaging, Article ID 409357, 15 pages, September, 2012.

[13] D. Nikic, J. Wu, P. Pauca, R. Plemmons, and Q. Zhang, "A novel approach to environment reconstruction in LiDAR and HSI data sets," Advanced Maui Optical and Space Surveillance Technologies Conference (AMOS Tech., September, 2012), Maui, HI.

[14] X. Zhao, F. Wang, T. Huang, M. Ng and R. Plemmons, "Deblurring and Sparse Unmixing For Hyperspectral Images," IEEE Trans. on Geoscience and Remote Sensing 51(7-1), pp. 4045-4058 (2013).

[15] N. Gillis, R. Plemmons, "Sparse Nonnegative Matrix Underapproximation and its Application to Hyperspectral Image Analysis," Linear Algebra and its Applications, 438 (10), pp. 3991-4007 (2013).

[16] Q. Zhang, P. Pauca and R. Plemmons, "Randomized Methods in Lossless Compression of Hyperspectral Data," J. Applied Remote Sensing. 7(1), 074598 (2013).

[17] Q. Zhang, P. Pauca and R. Plemmons, "Joint Blind Deconvolution and Spectral Unmixing of Hyperspectral Images," Proc. Advanced Maui Optical and Space Surveillance Technologies Conference (AMOS Tech., September, 2013), Maui, HI.

[18] Q. Zhang and R. Plemmons, "Image Reconstruction from Double Random Projection," IEEE Trans. on Image Proc., 23(6), pp. 2501 - 2513, 2014.)

[19] S. Berisha, J. Nagy and R. Plemmons, "Deblurring and Sparse Unmixing of Hyperspectral Images using Multiple Point Spread Functions," SIAM J. Scientific Comp., in press, 2015.)

[20] S. Berisha, J. Nagy and R. Plemmons, "Estimation of Atmospheric PSF Parameters for Hyperspectral Imaging," Numerical Lin. Alg. and Applic., in press, 2015.)

[21] T.-H. Tsai and D. Brady, "Coded aperture snapshot spectral polarization imaging," Appl. Optics, vol. 52, pp. 2153-2161 (2013).

[22] X. Yuan, T. H. Tsai, R. Zhu, P. Llull, D. J. Brady, and L. Carin, "Compressive Hyperspectral Imaging with Side Information," IEEE J. Sel. Topics Signal Process 99 (2015)

[23] T. H. Tsai, X. Yuan, and D. J. Brady, "Spatial light modulator based color polarization imaging," accepted by Opt. Express (2015).

[24] R. Zhu, T. H. Tsai, and D. J. Brady, "Coded Aperture Snapshot Spectral Imager Based on Liquid Crystal Spatial Light Modulator," in Frontiers in Optics 2013, paper FW1D.4.

[25] T. H. Tsai, X. Yuan, L. Carin, and D. J. Brady, "Spatial Light Modulator Based Spectral Polarization Imaging," in Computational Optical Sensing and Imaging 2014, paper CW3C.4.

3 Patents

1. S. Prasad, "Rotating Point-Spread Function (PSF) Design for Three-Dimensional Imaging," filed with the US Patent and Trademark Office, Serial No. 14/202,915 (10 March 2014).